Journal of Materials Chemistry A

ROYAL SOCIETY OF CHEMISTRY

PAPER

View Article Online
View Journal | View Issue

Check for updates

Cite this: J. Mater. Chem. A, 2025, 13, 9479

High toluene uptake at a trace concentration in a novel gallium-based metal–organic framework†

Thach N. Tu,[a] Hyuk Taek Kwon,[b] Manfred Scheer *[c] and Jinsoo Kim *[a]

Received 28th November 2024
Accepted 23rd February 2025

DOI: 10.1039/d4ta08445d

rsc.li/materials-a

A novel gallium-based MOF, termed Ga-BPT$_{SC}$ (single crystal) and Ga-BPT$_P$ (powder), was synthesized. Structural analysis reveals that Ga-BPT$_{SC}$ and Ga-BPT$_P$ are isostructural with a slight difference in the unit cell parameters. Specifically, both Ga-BPT$_{SC}$ and Ga-BPT$_P$ are constructed from a trinuclear gallium oxide cluster and BPT^{3-} linker, consisting of a 3D structure with unique micro-channels decorated with small adsorption cavities (~6.5 Å). These structural features enable Ga-BPT$_P$ to adsorb a significant amount of toluene and xylenes at trace levels (toluene and xylene uptakes of 6.29 mmol g^{-1} at P/P_0 = 0.005 and ~6.1 mmol g^{-1} at P/P_0 = 0.01, respectively). The toluene uptake of Ga-BPT$_P$ exceeds that of the recently reported MOFs, ZJU-520 and ZJU-620, as well as benchmark MOFs (*e.g.* UiO-66 and HKUST-1) at P/P_0 = 0.005. Moreover, the breakthrough toluene capture of Ga-BPT$_P$ at 200 ppm reveals an uptake of 4.89 mmol g^{-1}, which is considerably higher than that of the benchmark MOFs (*e.g.* ZIF-8, MIL-100, MIL-101, UiO-66, HKUST-1 and UiO-66-NH$_2$). The development of the Ga-BPT synthetic protocol and its exceptional adsorption and separation capacities pave the way to the discovery and application of a new class of gallium-based MOFs constructed from trinuclear gallium oxide clusters.

Introduction

Metal–organic frameworks (MOFs) are a type of porous material, whose structures are based on chelating bonds between inorganic metal clusters and organic linkers with multi-topic chelation groups.[1] This principle endows MOFs with the possibility of being designed and synthesized by connecting modular building blocks to control the structure, pore size, shape, and surface polarity.[2] Currently, MOFs are employed in a wide range of applications, such as drug delivery,[3,4] crystalline sponges,[5–7] catalysis,[8–10] proton conduction,[11–14] chemical sensors,[15–17] and gas/vapor adsorption and separation.[18–22]

Gallium, located in Group 13 of the periodic table between aluminum and indium, commonly has an oxidation state of +3. Gallium-based MOFs exhibit unique properties for electrochemical catalysis,[23] and adsorption and/or separation of water, H_2, CO_2 and SF_6.[24–28] Specifically, gallium-based MOFs exhibit strong anti-bacterial and anti-inflammatory properties for drug applications and drug delivery.[29–33] Moreover, gallium–Rh clusters immobilized in MOFs are capable of complexation with alkenes.[34] Despite the wide availability of MOFs synthesized from Al^{3+} and In^{3+}, MOFs synthesized from Ga^{3+} are rare.[35–38] Currently, only a few studies have been devoted to exploring the structures and building motifs of MOFs from gallium clusters, with only a few Ga-based MOFs reported in the literature.[24–26,28,39–46] Furthermore, these structures primarily rely on $(Ga(OH)(CO_2)_2)_n$ rod-based metal clusters,[25,26,28,39–41,43] and tetrahedral/octahedral Ga^{3+} atoms.[24,42,44,45] Discovering synthetic protocols toward other gallium inorganic building blocks is challenging but would open up new opportunities in employing the unique properties of gallium-based MOFs for emerging applications.

Aromatic-based VOCs, such as toluene and xylenes, are a common class of organic substances used in various aspects of daily life and industrial production.[47] Despite this, these substances can cause severe harm to human health. For example, long-term exposure to toluene and xylenes is often associated with hearing disorders and neurological problems.[48] Recently, efforts have been made to synthesize and engineer the structures of MOFs to capture these compounds.[47,49–57] Despite the fact that MOFs usually exhibit considerable uptakes of these compounds at high relative pressure, developing MOFs with high uptakes at trace concentrations remains challenging.[48,49,54,55]

Herein, we report the first gallium-based MOFs synthesized from a trinuclear gallium oxide cluster, termed Ga-BPT$_{SC}$ (single crystal phase) and Ga-BPT$_P$ (powder phase). SCXRD structural analysis of Ga-BPT$_{SC}$ revealed a formula of $Ga_3O(BPT)_2$(-Ben)(H_2O), where BPT = biphenyl-3,4′,5-tricarboxylate and Ben

[a]Department of Chemical Engineering (Integrated Engineering), Kyung Hee University, 1732 Deogyeong-daero, Giheung-gu, Yongin-si, Gyeonggi-do 17104, Republic of Korea. E-mail: jkim21@khu.ac.kr

[b]Department of Chemical Engineering, Pukyong National University, 45 Yongso-ro, Nam-gu, Busan 48513, Republic of Korea

[c]Institute of Inorganic Chemistry, University of Regensburg, 93040 Regensburg, Germany. E-mail: Manfred.Scheer@chemie.uni-regensburg.de

† Electronic supplementary information (ESI) available. See DOI: https://doi.org/10.1039/d4ta08445d

= benzoate. Ga-BPT$_{SC}$ is built from $Ga_3O(CO_2)_7(H_2O)$ clusters stitched by the H_3BPT linker to realize a 3D structure with asymmetric 9.2 Å channels. Meanwhile, Ga-BPT$_P$ possesses a similar structure to Ga-BPT$_{SC}$, but with a slight change of the unit cell parameters. Interestingly, the micropore channels of Ga-BPT$_P$ feature four different adsorption sites matching the molecule size of aromatic compounds such as toluene. The high density of binding sites leads to an exceptionally high toluene uptake of ~6.3 mmol g^{-1} (0.58 g g^{-1}) at the trace concentration of $P/P_0 = 0.005$ (~200 ppm), which surpasses the recently reported values of ZJU-520,[58] ZJU-620,[50] UiO-66,[59] and HKUST-1.[60] Ga-BPT$_P$ exhibited a high breakthrough toluene capacity of 4.98 mmol g^{-1} (0.46 g g^{-1}) at 200 ppm and 25 °C, which is much higher than that of benchmark MOFs such as HKUST-1, UiO-66, UiO-66-NH_2, MIL-100, MIL-101, and ZIF-8.

Experimental

Synthesis of Ga-BPT$_{SC}$

A mixture of GaI (5.6 mg, 0.028 mmol), H_3BPT (2.4 mg, 0.009 mmol), and benzoic acid (24 mg, 0.197 mmol) was weighed into a Pyrex tube. DMF (1.5 mL) was then added to completely dissolve the mixture. The tube was then isothermally heated at 180 °C for 72 h to yield needle-like single crystals (Ga-BPT$_{SC}$) attached to the tube wall (above the DMF level) and a white powder product at the tube bottom (Ga-BPT$_P$).

Synthesis of Ga-BPT$_P$

A similar procedure is employed; however, a larger scale of Ga-BPT$_P$ was synthesized using a Teflon line stainless steel reactor. In detail, a mixture of GaI (336 mg, 1.71 mmol), H_3BPT (144 mg, 0.5 mmol), and benzoic acid (1.44 g, 0.012 mol) was weighed into a Teflon-lined Hydrothermal Autoclave. DMF (48 mL) was then added to completely dissolve the mixture. Subsequently, the autoclave was isothermally heated at 180 °C in a circulated oven for 48 h. The product as a white powder was then collected, solvent exchanged and outgassed under freeze-drying conditions, followed by heating at 150 °C under dynamic vacuum to obtain ~150 mg (~30% yield) of activated Ga-BPT$_P$. EA (activated sample): calcd for $Ga_3C_{37}H_{21}O_{16}$ =$Ga_3O(C_{15}H_7O_6)_2(C_7H_5O_2)(H_2O)\cdot 8H_2O$: C, 41.4; H, 3.5%. Found: C, 41.23; H, 3.1; N, 0.1948%.

The breakthrough experiments

The breakthrough experiments were performed utilizing an in-house system. The flow rate was controlled by a mass flow control (MFC, Brooks instruments, model 5800E). Before the breakthrough experiments, the mass flow controllers (MFCs) were calibrated using a bubble film flowmeter (Fig. S13†). The stream after passing through the column was analyzed using a mass spectrometry analyzer (Hidden Analytical, QGA).

Breakthrough capture of toluene

~10 mg Ga-BPT$_P$ (or the reference MOFs) was added into the columns (length: 65 mm and inner diameter: 6 mm). The columns were then filled with glass beads to minimize the dead volume. Finally, glass wool was placed at both ends of the columns. The columns were then connected to the mass flow controllers (MFCs). Toluene (200 ppm) in argon was then fed into the column at a flow rate of ~7.4 cm^3 min^{-1} (at 25 °C and under ambient pressure). After adsorption, the Ga-BPT$_P$ column was regenerated overnight under dynamic vacuum at 150 °C.

Results and discussion

Ga-BPT$_{SC}$ was synthesized using a seal tube procedure. The seal tube containing a DMF solution (~1.5 mL) of H_3BPT and GaI was isothermally heated at 180 °C for 72 h in the presence of a benzoic acid modulator. The tube was then cooled naturally to room temperature. The reaction led to a white powder product at the bottom and colourless needle-like single crystals attached to the tube wall above the liquid level. The needle-like crystals were then collected for single-crystal X-ray diffraction (SCXRD) to determine their crystal structure (Section S2†). Ga-BPT$_{SC}$ was found to crystallise in the acentric orthorhombic space group, $Pmn2_1$ (No. 31), with unit cell parameters, $a = 22.997$, $b = 9.7823$, and $c = 15.749$ Å (CCDC number 2386132, Table S1†). The structure of Ga-BPT$_{SC}$ is built from trinuclear gallium oxide clusters with six carboxylate extension points connected by the asymmetric BPT^{3-} linkers and one extension point coordinated by a benzoate molecule (Fig. 1a and b). This arrangement realizes a three-dimensional structure with an asymmetric one-dimensional channel of 9.2 Å featuring a lining of coordinated benzoate at a fixed distance to form adsorption cavities of 6.5 Å (Fig. 1c and d).

The PXRD pattern of Ga-BPT$_P$ (powder product) was collected. However, the patterns indicated a slight shift of the (1 0 1) peak to a smaller angle compared with the simulated PXRD from the single-crystal X-ray diffraction structure of Ga-BPT$_{SC}$ (Fig. 2a). We deduced the above difference to be due to the slight change of the unit cell parameters of Ga-BPT$_P$. To further clarify the structure of Ga-BPT$_P$, the PXRD patterns of Ga-BPT$_P$ were monitored upon slowly drying from DMF. The PXRD pattern of Ga-BPT$_P$ after drying from DMF exhibited a slight peak shift to match with the simulated PXRD pattern of Ga-BPT$_{SC}$ (Fig. S8†). We further collected the PXRD patterns of the activated sample for Rietveld refinement (Section S3†). The model structure of Ga-BPT$_P$ was then built based on the structure of Ga-BPT$_{SC}$; however, with a change of the unit cell parameters ($a = 22.042$; $b = 9.896$; $c = 17.960$ Å). The Rietveld refinement of this modelled structure was performed using Material studio software to optimize the atomic positions within the lattice. The structure successfully converged with satisfactory R-values ($2\theta = 2$–$50°$, $R_p = 2.39\%$, and $R_{wp} = 4.51\%$), as shown in Fig. 2b and Table S2.†[61,62] The refined structure clearly reveals a similar, but slightly larger unit cell parameter compared to Ga-BPT$_{SC}$, resulting in a slightly larger channel of Ga-BPT$_P$ (~10 Å) (Fig. 2c).

We further characterized Ga-BPT$_P$ by common methods (Section S4†). Fourier transform infrared (FTIR) spectroscopy analysis of the activated Ga-BPT$_P$ showed the C–O stretching band of coordinated carboxylate at 1640 and 1610 cm^{-1} (multi-carboxylate peaks are caused by the presence of an asymmetric linker or different linkers in Ga-BPT$_P$) indicating the stability of

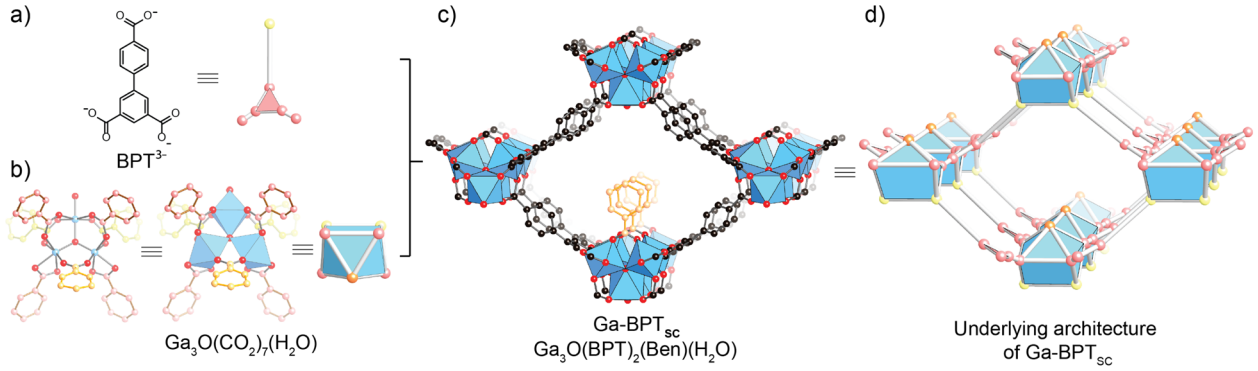

Fig. 1 Crystal structure of Ga-BPT_{SC} (c) is constructed from the BPT^{3-} linker (a) and the trinuclear gallium oxide $Ga_3O(CO_2)_7(H_2O)$ cluster (b) and the representation of the underlying architecture of Ga-BPT_{SC} (d). Atom colors: Ga, blue balls and polyhedra; C, black; O, red. All other H atoms are omitted for clarity.

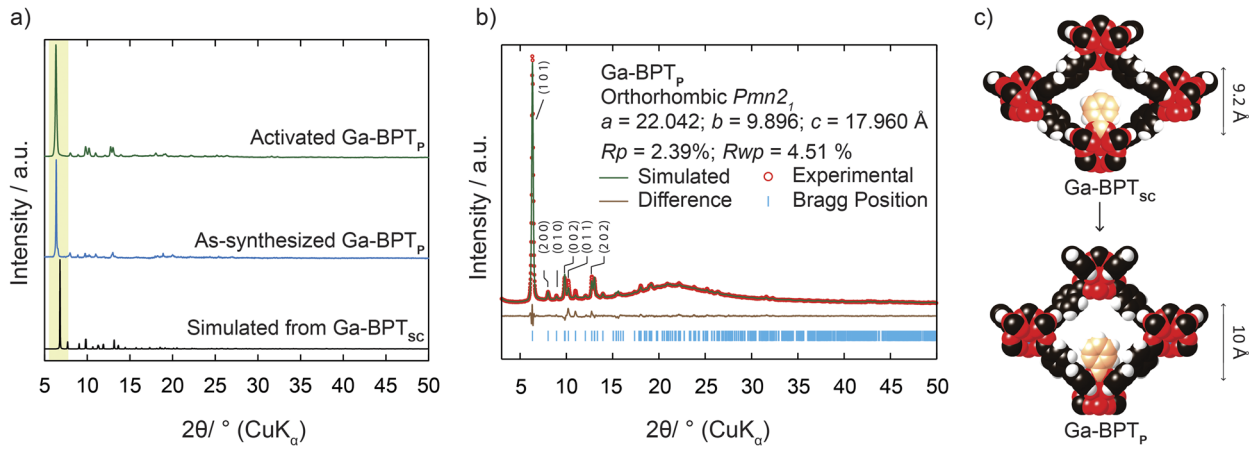

Fig. 2 Structural analysis of Ga-BPT_P: PXRD patterns of Ga-BPT_P in comparison to the simulated pattern of Ga-BPT_{SC} (a); the experimental (red) and refined (green) PXRD patterns of as-synthesized Ga-BPT_P after Rietveld refinement with the difference plot (brown) and Bragg positions (blue) are also provided (b); the structural difference between Ga-BPT_P and Ga-BPT_{SC} (c).

the atomic connectivity upon activation (Fig. S2†). N_2 adsorption measurement at 77 K was performed to analyse the porosity and the surface area of Ga-BPT_P. The resulting isotherm indicated reversible uptake with a BET (Langmuir) surface area of 2264 $m^2\ g^{-1}$ (2427 $m^2\ g^{-1}$), which is in line with the theoretical value (~2800 $m^2\ g^{-1}$) (Fig. S5–S7†). The well-matched PXRD pattern of the activated Ga-BPT_P with that from the as-synthesized sample (Fig. 2a) and the high porosity confirmed the stability of Ga-BPT_P upon activation. Elemental microanalysis (EA) confirmed the proposed chemical formula from the single crystal X-ray diffraction model of Ga-BPT_{SC} to be $Ga_3O(C_{15}H_7O_6)_2(C_7H_5O_2)(H_2O)\cdot 8H_2O$ (cal. C, 41.4; H, 3.5%. Found: C, 41.23; H, 3.1; N, 0.1948%). Thermogravimetric analysis (TGA) indicated stability up to 350 °C (Fig. S3†). Moreover, the resulting Ga_2O_3 (~36 wt%) matches well with the calculated value from the structural model (~31 wt%). FE-SEM also revealed the square cylinder morphology of the Ga-BPT_P crystals (size ~0.9 × 1.3 μm) (Fig. S4†).

The high surface area and the dense existence of potential binding sites in Ga-BPT_P drove us to analyse its adsorption properties *versus* guest molecules of suitable molecular size. The toluene adsorption isotherm of Ga-BPT_P at 25 °C was measured, which demonstrates an increasing step of the uptake at an exceptionally low pressure (P/P_0 from 0.0015, P_0 = 3.82 kPa) to reach the uptake capacity of 6.29 mmol g^{-1} (or 0.58 g g^{-1}) at $P/P_0 = 0.005$, which corresponds to an absolute pressure of 0.02 kPa (or 200 ppm) (Fig. 3a). Noticeably, this value of toluene concentration ($P/P_0 = 0.005$) is just right at the legal airborne permissible exposure limit for toluene according to the regulation from the U.S. Department of Labour.[48] The high toluene uptake at low pressure indicated the strong interaction of Ga-BPT_P and toluene. At $P/P_0 > 0.005$, the toluene uptake was found to gradually increase and reach the maximum capacity of 8.75 mmol g^{-1} at P/P_0 ~0.96 (Fig. 3a). Despite the lack of available toluene adsorption data at low pressure from the literature, we found that the toluene uptake of Ga-BPT_P exceeded that of the recently reported toluene uptakes at $P/P_0 = 0.005$ (Table 1).

The high toluene uptake at trace toluene concentration (6.29 mmol g^{-1} at $P/P_0 = 0.005$) drove us to investigate its adsorption mechanism in Ga-BPT_P. The toluene uptake of ~11 molecules per unit cell was chosen (~6 mmol g^{-1}) to probe the

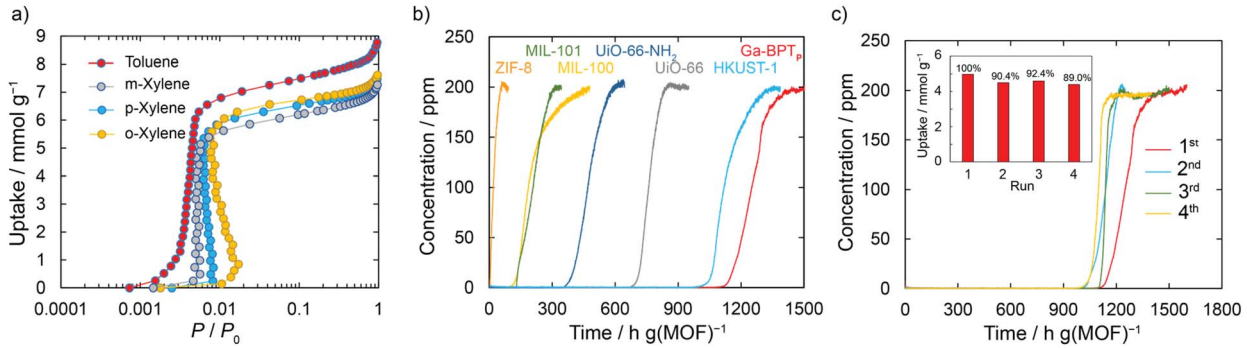

Fig. 3 Adsorption analysis of Ga-BPT$_P$ with the toluene and xylene adsorption isotherms (a); the breakthrough capture of toluene (b); and the regeneration of Ga-BPT$_P$ (c).

Table 1 Static trace toluene uptake of Ga-BPT$_P$ in comparison with other MOFs

Material	Uptake @ 0.02 kPa (mmol g^{-1})	Reference
Ga-BPT$_P$	6.29	This work
ZJU-520	0.27	58
ZJU-620	2.0	50
BUT-66	1.36	54
UiO-66	3.22	59
HKUST-1	4.36	60

potential binding sites by Grand Canonical Monte Carlo (GCMC) simulation. The results from the GCMC simulation revealed toluene adsorption sites (Fig. 4, S11 and S12†). These sites are named: site I (~6.5 Å) – confined between the coordinated benzoate and the channel walls; site II (~6.5 Å) – confined between the gallium unsaturated metal site, the Ga clusters and the linkers; site III (~5.0 × 7.0 Å) – confined between the two BPT^{3-} and the coordinated benzoate; site IV (~4 Å) – confined between the coordinated benzoate and the isophthalate ring of BPT^{3-}. The matching sizes facilitated the strong binding and high uptake of toluene *via* π–π and CH–π interaction at sites I, II, IV, and the Ga–π and/or Ga–CH at site II (Fig. S12†).

We further measured the Ga-BPT$_P$ adsorption isotherms of *o*, *p*, and *m*-xylenes at 25 °C (Fig. 3a). All of these compounds exhibited strong interaction with Ga-BPT$_P$ evidenced by their high uptake at low pressure. Accordingly, the adsorption isotherms of the three xylene compounds showed an increasing step to reach similar uptakes of ~6.1 mmol g^{-1} at P/P_0 ~0.01 (with $P_{0,\ o\text{-xylene}} = 0.888$; $P_{0,\ p\text{-xylene}} = 1.168$; $P_{0,\ m\text{-xylene}} = 1.108$), which are equal to that of toluene uptake at $P/P_0 = 0.005$ (Fig. 3a). In a similar manner, gradual increases of xylene uptake were found at $P/P_0 > 0.01$ to reach the maximum capacity of ~7 mmol g^{-1} at P/P_0 ~0.96. The increasing step of xylene uptake at low pressure could be attributed to the adsorption at the active sites in Ga-BPT$_P$.

In the next step, the breakthrough performance of Ga-BPT$_P$ for toluene capture at trace levels was evaluated (Section S7†). As the legal airborne permissible exposure limit for toluene must be below 200 ppm for an average 8 h work shift and should not exceed 500 ppm in a 10 min work period, the toluene concentration of 200 ppm was chosen as a controlled target.[48] An argon stream containing 200 ppm toluene was passed through the Ga-BPT$_P$ column at the flow rate of 7.4 mL min^{-1}. The toluene breakthrough curve of Ga-BPT$_P$ was recorded with the output concentration of toluene in ppm as the O*y* axis and the time normalized to the mass of Ga-BPT$_P$ as the O*x* axis (Fig. 3b). The breakthrough curve at 25 °C showed that the toluene concentration broke through at 1, 20, and 200 ppm after ~1100, 1160, and 1493 h g^{-1}, corresponding to the uptakes of 4.42, 4.62, and 4.98 mmol g^{-1}, respectively.

We further investigated the toluene breakthrough capture of the benchmark MOFs for comparison (ZIF-8, MIL-100, MIL-101, UiO-66, and UiO-66-NH$_2$) (Fig. 3b). The toluene breakthrough uptakes corresponding to the concentrations of 1, 20, and

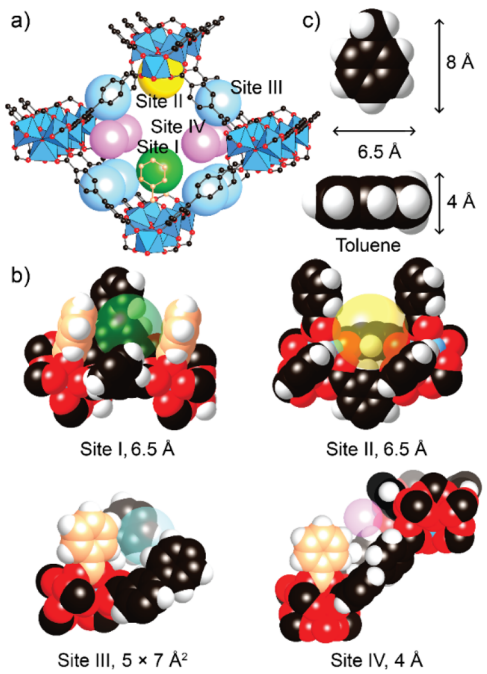

Fig. 4 The adsorption sites in Ga-BPT$_P$ suggested by the GCMC simulation: adsorption cavities in Ga-BPT$_P$ (a and b); and the molecule size of toluene (c).

Table 2 Breakthrough toluene uptake of Ga-BPT_P and benchmark materials

Materials	Toluene breakthrough uptake (mmol g^{-1})		
	@ 1 ppm	@ 20 ppm	@ 200 ppm
Ga-BPT_P	4.42	4.62	4.98
HKUST-1	3.98	4.23	4.50
UiO-66	2.69	2.86	3.37
UiO-66-NH_2	1.43	1.61	1.88
MIL-100	0.4	0.55	0.85
MIL-101	0.52	0.55	0.83
ZIF-8	0.011	0.022	0.076

200 ppm are listed in Table 2. Accordingly, UiO-66 and HKUST-1 exhibited the uptakes of 3.37 and 4.5 mmol g^{-1} at 200 ppm, which well-agreed with the uptake values from the toluene isotherms at $\sim P/P_0 = 0.005$ (3.22 and 4.36 mmol g^{-1}, respectively).[59,60] Remarkably, it was found that the breakthrough toluene uptake of Ga-BPT_P exceeded that of HKUST-1, UiO-66, and other benchmark MOFs (Table 2).

The durability of Ga-BPT_P for breakthrough toluene capture was further evaluated by recycling under vacuum at 150 °C. The breakthrough experiments showed that Ga-BPT_P could be recycled without significantly reducing the uptake performance. Specifically, Ga-BPT_P maintains up to 89% of the original toluene uptake capacity after the 4th regeneration (Fig. 3c). The structural maintenance of Ga-BPT_P after completing the 4th-cycle of regeneration for toluene capture was also confirmed using PXRD analysis, which showed a high degree of correspondence with the original sample (Fig. S15†). The dependence of Ga-BPT_P's toluene breakthrough on temperature was investigated to evaluate the dynamic uptake capacities under varying temperature conditions (Fig. S16†). The results indicated a slight decrease in uptake capacity with an increase in temperature from RT to 40 °C, retaining ~86% of the toluene uptake observed at RT. These results demonstrate the excellent performance of Ga-BPT_P in capturing toluene under fluctuating temperature conditions. Moreover, Ga-BPT_P exhibited good performance in the presence of moisture, maintaining 85% of its toluene uptake capacity compared to dry conditions under continuing flow at 20% RH (Fig. S17†), which is in agreement with the condensed RH at 32% from the water adsorption isotherm (Fig. S9†).

Conclusion

A novel gallium-based MOF constructed from trinuclear gallium oxide clusters and a BPT^{3-} linker was synthesized and characterized for the first time. The unique micro-channels, decorated with small adsorption cavities and active sites, allow Ga-BPT_P to exhibit high toluene and xylene uptake capacities at trace levels. The volumetric toluene uptake of Ga-BPT_P at $P/P_0 = 0.005$ exceeded the recently reported toluene uptakes of ZJU-520, ZJU-620, BUT-66 and the benchmark MOFs (UiO-66 and HKUST-1) at the same pressure. Similarly, Ga-BPT_P exhibited an exceptional capacity for breakthrough toluene capture at 200 ppm (4.98 mmol g^{-1}), which is much higher than that of benchmark MOFs such as UiO-66, UiO-66-NH_2, MIL-100, MIL-101, ZIF-8 and HKUST-1.

Data availability

Data supporting this study are included within the article and/or ESI.†

Author contributions

T. N. T. conceived the idea, designed and conducted the experiments, interpreted the data, and wrote the paper. H. T. K. measured the adsorption isotherms. J. K. and M. S. supervised the work. T. N. T. and J. K. secured the funding. All authors contributed to reviewing, editing, and revising the paper.

Conflicts of interest

The authors declare no competing interests.

Acknowledgements

This work was supported by the Brainpool Program through the National Research Foundation of Korea (NRF), funded by the Ministry of Science and ICT, Republic of Korea (NRF 2022H1D3A2A02079453). T. N. T. and M. S. acknowledge the support from the Alexander von Humboldt Foundation for Ga-BPT_{SC} synthesis and structural determination.

References

1 T. N. Tu, M. V. Nguyen, H. L. Nguyen, B. Yuliarto, K. E. Cordova and S. Demir, *Coord. Chem. Rev.*, 2018, **364**, 33–50.
2 H. Furukawa, K. E. Cordova, M. O'Keeffe and O. M. Yaghi, *Science*, 2013, **341**, 974–986.
3 S. Haddad, I. Abánades Lázaro, M. Fantham, A. Mishra, J. Silvestre-Albero, J. W. M. Osterrieth, G. S. Kaminski Schierle, C. F. Kaminski, R. S. Forgan and D. Fairen-Jimenez, *J. Am. Chem. Soc.*, 2020, **142**, 6661–6674.
4 W. Cai, J. Wang, C. Chu, W. Chen, C. Wu and G. Liu, *Adv. Sci.*, 2019, **6**, 1801526.
5 T. N. Tu and M. Scheer, *Chem*, 2023, **9**, 227–241.
6 Y. Wada, P. M. Usov, B. Chan, M. Mukaida, K. Ohmori, Y. Ando, H. Fuwa, H. Ohtsu and M. Kawano, *Nat. Commun.*, 2024, **15**, 81.
7 S. Y. Zhang, D. Fairen-Jimenez and M. J. Zaworotko, *Angew. Chem., Int. Ed.*, 2020, **59**, 17600–17606.
8 T. N. Tu, S. A. Khalate, K. Chang and J. Kim, *J. Mater. Chem. A*, 2024, **12**, 7622.
9 S. H. Doan, N. K. Q. Tran, P. H. Pham, V. H. H. Nguyen, N. N. Nguyen, P. T. M. Ha, S. Li, H. V. Le, N. T. H. Le, T. N. Tu and N. T. S. Phan, *Eur. J. Org. Chem.*, 2019, **2019**, 2382–2389.

10 T. A. To, Y. H. Vo, H. T. T. Nguyen, P. T. M. Ha, S. H. Doan, T. L. H. Doan, S. Li, H. V. Le, T. N. Tu and N. T. S. Phan, *J. Catal.*, 2019, **370**, 11–20.
11 T. N. Tu, N. Q. Phan, T. T. Vu, H. L. Nguyen, K. E. Cordova and H. Furukawa, *J. Mater. Chem. A*, 2016, **4**, 3638–3641.
12 P. Ramaswamy, N. E. Wong and G. K. H. Shimizu, *Chem. Soc. Rev.*, 2014, **43**, 5913–5932.
13 M. V. Nguyen, T. H. N. Lo, L. C. Luu, H. T. T. Nguyen and T. N. Tu, *J. Mater. Chem. A*, 2018, **6**, 1816–1821.
14 T. H. N. Lo, M. V. Nguyen and T. N. Tu, *Inorg. Chem. Front.*, 2017, **4**, 1509–1516.
15 W. Bin Li, Y. Wu, X. F. Zhong, X. H. Chen, G. Liang, J. W. Ye, Z. W. Mo and X. M. Chen, *Angew. Chem., Int. Ed.*, 2023, **62**, e202303500.
16 H. Zhang, Z. J. Ding, Y. H. Luo, W. Y. Geng, Z. X. Wang and D. E. Zhang, *CrystEngComm*, 2022, **24**, 667–673.
17 S. Srivastava, B. K. Gupta and R. Gupta, *Cryst. Growth Des.*, 2017, **17**, 3907–3916.
18 T. N. Tu, Y. Shin, S. A. Khalate, K. Chang, H. T. Kwon and J. Kim, *Sep. Purif. Technol.*, 2024, **343**, 127128.
19 T. N. Tu, H. T. D. Nguyen and N. T. Tran, *Inorg. Chem. Front.*, 2019, **6**, 2441–2447.
20 M. I. Gonzalez, M. T. Kapelewski, E. D. Bloch, P. J. Milner, D. A. Reed, M. R. Hudson, J. A. Mason, G. Barin, C. M. Brown and J. R. Long, *J. Am. Chem. Soc.*, 2018, **140**, 3412–3422.
21 A. Henrique, T. Maity, H. Zhao, P. F. Brântuas, A. E. Rodrigues, F. Nouar, A. Ghoufi, G. Maurin, J. A. C. Silva and C. Serre, *J. Mater. Chem. A*, 2020, **8**, 17780–17789.
22 H. Wang, X. Dong, J. Lin, S. J. Teat, S. Jensen, J. Cure, E. V. Alexandrov, Q. Xia, K. Tan, Q. Wang, D. H. Olson, D. M. Proserpio, Y. J. Chabal, T. Thonhauser, J. Sun, Y. Han and J. Li, *Nat. Commun.*, 2018, **9**, 1745.
23 Y. Gao, H. Xiao, X. Ma, Z. Yue, C. Liu, M. Zhao, L. Zhang, J. Zhang, E. Luo, T. Hu, B. Lv, J. Jia and H. Wu, *J. Mater. Chem. A*, 2024, **12**, 8272–8280.
24 D. Banerjee, S. J. Kim, H. Wu, W. Xu, L. A. Borkowski, J. Li and J. B. Parise, *Inorg. Chem.*, 2011, **50**, 208–212.
25 C. Volkringer, M. Meddouri, T. Loiseau, N. Guillou, J. Marrot, G. Férey, M. Haouas, F. Taulelle, N. Audebrand and M. Latroche, *Inorg. Chem.*, 2008, **47**, 11892–11901.
26 M. Åhlén, Y. Zhou, D. Hedbom, H. S. Cho, M. Strømme, O. Terasaki and O. Cheung, *J. Mater. Chem. A*, 2023, **11**, 26435–26441.
27 F. X. Coudert, A. U. Ortiz, V. Haigis, D. Bousquet, A. H. Fuchs, A. Ballandras, G. Weber, I. Bezverkhyy, N. Geoffroy, J. P. Bellat, G. Ortiz, G. Chaplais, J. Patarin and A. Boutin, *J. Phys. Chem. C*, 2014, **118**, 5397–5405.
28 C. P. Krap, R. Newby, A. Dhakshinamoorthy, H. García, I. Cebula, T. L. Easun, M. Savage, J. E. Eyley, S. Gao, A. J. Blake, W. Lewis, P. H. Beton, M. R. Warren, D. R. Allan, M. D. Frogley, C. C. Tang, G. Cinque, S. Yang and M. Schröder, *Inorg. Chem.*, 2016, **55**, 1076–1088.
29 Y. Xie, Z. H. Jiao, J. Dong, S. L. Hou and B. Zhao, *Inorg. Chem.*, 2023, **62**, 5168–5175.
30 F. Shi, S. S. Ma, S. Liu, R. Xin, B. Chen, W. Ye and J. Sun, *Colloids Interface Sci. Commun.*, 2023, **56**, 100735.
31 G. Song, M. Li, B. Zhou, H. Qi and J. Guo, *Heliyon*, 2024, **10**, e31788.
32 K. Huang, J. Wang, Q. Zhang, K. Yuan, Y. Yang, F. Li, X. Sun, H. Chang, Y. Liang, J. Zhao, T. Tang and S. Yang, *Adv. Funct. Mater.*, 2022, **32**, 2204906.
33 S. Liu, Y. Ji, H. Zhu, Z. Shi, M. Li and Q. Yu, *J. Mater. Chem. B*, 2023, **11**, 10446–10454.
34 S. P. Desai, J. Ye, J. Zheng, M. S. Ferrandon, T. E. Webber, A. E. Platero-Prats, J. Duan, P. Garcia-Holley, D. M. Camaioni, K. W. Chapman, M. Delferro, O. K. Farha, J. L. Fulton, L. Gagliardi, J. A. Lercher, R. L. Penn, A. Stein and C. C. Lu, *J. Am. Chem. Soc.*, 2018, **140**, 15309–15318.
35 L. M. Aguirre-Díaz, D. Reinares-Fisac, M. Iglesias, E. Gutiérrez-Puebla, F. Gándara, N. Snejko and M. Á. Monge, *Coord. Chem. Rev.*, 2017, **335**, 1–27.
36 T. Steenhaut, Y. Filinchuk and S. Hermans, *J. Mater. Chem. A*, 2021, **9**, 21483–21509.
37 Y.-J. Song, Y.-H. Zuo, Z. Li and G. Li, *Inorg. Chem. Front.*, 2024, **11**, 7256–7295.
38 Y. Liu, J. F. Eubank, A. J. Cairns, J. Eckert, V. C. Kravtsov, R. Luebke and M. Eddaoudi, *Angew. Chem., Int. Ed.*, 2007, **46**, 3278–3283.
39 Y. Zhang, B. E. G. Lucier, S. M. McKenzie, M. Arhangelskis, A. J. Morris, T. Friščić, J. W. Reid, V. V. Terskikh, M. Chen and Y. Huang, *ACS Appl. Mater. Interfaces*, 2018, **10**, 28582–28596.
40 R. Hajjar, C. Volkringer, T. Loiseau, N. Guillou, J. Marrot, G. Férey, I. Margiolaki, G. Fink, C. Morais and F. Taulelle, *Chem. Mater.*, 2011, **23**, 39–47.
41 J. Benecke, A. Fuß, T. A. Engesser, N. Stock and H. Reinsch, *Eur. J. Inorg. Chem.*, 2021, **2021**, 713–719.
42 G. Chaplais, A. Simon-Masseron, F. Porcher, C. Lecomte, D. Bazer-Bachi, N. Bats and J. Patarin, *Phys. Chem. Chem. Phys.*, 2009, **11**, 5241–5245.
43 T. Rhauderwiek, S. Waitschat, S. Wuttke, H. Reinsch, T. Bein and N. Stock, *Inorg. Chem.*, 2016, **55**, 5312–5319.
44 G. Skorupskii, G. Chanteux, K. N. Le, I. Stassen, C. H. Hendon and M. Dincă, *Ann. N. Y. Acad. Sci.*, 2022, **1518**, 226–230.
45 L. Kobera, J. Havlin, S. Abbrent, J. Rohlicek, M. Streckova, T. Sopcak, V. Kyselova, J. Czernek and J. Brus, *Inorg. Chem.*, 2020, **59**, 13933–13941.
46 C. Volkringer, T. Loiseau, G. Férey, C. M. Morais, F. Taulelle, V. Montouillout and D. Massiot, *Microporous Mesoporous Mater.*, 2007, **105**, 111–117.
47 K. Vellingiri, P. Kumar, A. Deep and K. H. Kim, *Chem. Eng. J.*, 2017, **307**, 1116–1126.
48 T. N. Tu, T. M. Pham, Q. H. Nguyen, N. T. Tran, V. N. Le, L. H. Ngo, K. Chang and J. Kim, *Sep. Purif. Technol.*, 2024, **333**, 125883.
49 Y. Han, Y. Chen, Y. Ma, J. Bailey, Z. Wang, D. Lee, A. M. Sheveleva, F. Tuna, E. J. L. McInnes, M. D. Frogley, S. J. Day, S. P. Thompson, B. F. Spencer, M. Nikiel, P. Manuel, D. Crawshaw, M. Schröder and S. Yang, *Chem*, 2023, **9**, 739–754.

50 L. Hu, W. Wu, L. Gong, H. Zhu, L. Jiang, M. Hu, D. Lin and K. Yang, *Angew. Chem., Int. Ed.*, 2023, **62**, e202215296.
51 L. Chen, X. Wang, Z. Rao, Z. Tang, G. Shi, Y. Wang, G. Lu, X. Xie, D. Chen and J. Sun, *Appl. Catal., B*, 2022, **303**, 120885.
52 P. Li, S. Kim, J. Jin, H. C. Do and J. H. Park, *Appl. Catal., B*, 2020, **263**, 118284.
53 S. He, Q. Rong, H. Niu and Y. Cai, *Appl. Catal., B*, 2019, **247**, 49–56.
54 L. H. Xie, X. M. Liu, T. He and J. R. Li, *Chem*, 2018, **4**, 1911–1927.
55 T. He, X. J. Kong, Z. X. Bian, Y. Z. Zhang, G. R. Si, L. H. Xie, X. Q. Wu, H. Huang, Z. Chang, X. H. Bu, M. J. Zaworotko, Z. R. Nie and J. R. Li, *Nat. Mater.*, 2022, **21**, 689–695.
56 Y. Wu, H. Chen, D. Liu, J. Xiao, Y. Qian and H. Xi, *ACS Appl. Mater. Interfaces*, 2015, **7**, 5775–5787.
57 T. N. Tu, N. T. Tran, Q. H. Nguyen, V. N. Le and J. Kim, *Korean J. Chem. Eng.*, 2024, **41**, 2461.
58 L. Hu, W. Wu, M. Hu, L. Jiang, D. Lin, J. Wu and K. Yang, *Nat. Commun.*, 2024, **15**, 3204.
59 G. Jajko, J. J. G. Sevillano, S. Calero, W. Makowski and P. Kozyra, *J. Phys. Chem. Lett.*, 2023, **14**, 5618–5623.
60 S. Li, S. Subhan, L. Zhou, J. Li, Z. Zhao and Z. Zhao, *Chem. Eng. J.*, 2023, **465**, 142791.
61 H. T. T. Nguyen, T. N. Tu, M. V. Nguyen, T. H. N. Lo, H. Furukawa, N. N. Nguyen and M. D. Nguyen, *ACS Appl. Mater. Interfaces*, 2018, **10**, 35462–35468.
62 T. N. Tu, H. T. T. Nguyen, H. T. D. Nguyen, M. V. Nguyen, T. D. Nguyen, N. T. Tran and K. T. Lim, *RSC Adv.*, 2019, **9**, 16784–16789.